Peer reviewed version

University of Bristol - Explore Bristol Research
General rights

Lagrangian wall shear stress structures and near wall transport in high Schmidt aneurysmal flows

Amirhossein Arzani[1] Alberto M. Gambaruto[2] Guoning Chen[3] and Shawn C. Shadden[1]†

[1]Mechanical Engineering, University of California Berkeley, Berkeley, CA, USA
[2]Mechanical Engineering, University of Bristol, Bristol, UK
[3]Computer Science, University of Houston, Houston, TX, USA

The wall shear stress (WSS) vector field provides a signature for near wall convective transport, and can be scaled to obtain a first order approximation of the near wall fluid velocity. The near wall flow field governs mass transfer problems in convection dominated open flows with high Schmidt number, in which case a flux at the wall will lead to a thin concentration boundary layer. Such near wall transport is of particular interest in cardiovascular flows whereby hemodynamics can initiate and progress biological events at the vessel wall. In this study we consider mass transfer processes in pulsatile blood flow of abdominal aortic aneurysms resulting from complex WSS patterns. Specifically, the Lagrangian surface transport of a species released at the vessel wall was advected in forward and backward time based on the near wall velocity field. Exposure time and residence time measures were defined to quantify accumulation of trajectories, as well as the time required to escape the near wall domain. The effect of diffusion and normal velocity was investigated. The trajectories induced by the WSS vector field were observed to form attracting and repelling coherent structures that delineated species distribution inside the boundary layer consistent with exposure and residence time measures. The results indicate that Lagrangian wall shear stress structures can provide a template for near wall transport.

1. Introduction

Wall shear stress (WSS) is the tangential component of traction on the wall. WSS provides two types of information. First, it can be used to quantify the frictional drag force per unit area on the wall. Second, it provides a first order approximation for near wall convective transport. In the context of mass or heat transfer, the importance of near wall flow is emphasized in high Schmidt (Sc) or high Prandtl (Pr) open flows with a flux of species concentration or heat at the wall, and a convection dominated free stream carrying a specific species concentration or temperature over the no-slip boundary. In this paper, we focus on high Sc mass transfer, however, the ideas could be used in high Pr heat transfer applications as well.

Mass transfer in the cardiovascular system, including the transport of solutes (e.g. oxygen and nutrients) or that of proteins and cells (e.g. low density lipids and blood cells), represents an important application of high Sc flows (Ethier 2002). The methods

† Email address for correspondence: shadden@berkeley.edu

presented herein will be applied to pulsatile blood flow inside abdominal aortic aneurysm (AAA). AAA is a permanent widening of the aorta in the abdominal region. The sudden expansion of the aorta, complex vascular anatomy, presence of branch arteries, and pulsatility of blood flow together lead to complex flow inside AAAs (Finol & Amon 2001; Deplano *et al.* 2007; Arzani & Shadden 2012), accompanied with complex WSS distributions (Salsac *et al.* 2006) and particle residence times (Suh *et al.* 2011*a,b*).

It is known that in convection dominated flows, a flux of species concentration at the wall will lead to the formation of a thin concentration boundary layer. The common approach to obtain the species concentration distribution is to solve the advection diffusion equation in an Eulerian framework. However, this approach requires an extremely high resolution near the wall, often leading to numerical difficulties in complex 3D flows (Ethier 2002). Alternatively, in the case of high *Sc* flows, the near wall region can be considered isolated from the rest of the flow, with the core flow having negligible *direct* effect on the concentration distribution. Because the WSS vector field can be scaled to obtain a first order approximation for the velocity vector field next to the wall, it may be used to compute surface-bound trajectories representing the transport of a material species near the wall. In the case of high *Sc* numbers, the concentration boundary layer is very thin, making this first order approximation reasonable for understanding near wall transport.

Previous studies have shown that for a prescribed concentration (Dirichlet boundary condition) on the wall, the resulting flux of concentration from the wall is mostly independent of the chaotic flow away from the wall (Ghosh *et al.* 1998). The observation that the boundary layer distribution of a concentration is largely unaffected by advection far from the wall motivates a reduced-order, near-wall approach, which can be based on the WSS vector field. It should be noted however that the large scale core flow features determine the WSS patterns (El Hassan *et al.* 2013), therefore the near wall transport depends on the flow topology away from the wall indirectly.

In prior work, critical points of the WSS vector field and their dynamics have been observed to play an important role in organizing near wall transport (Perry & Chong 1987; Cardesa *et al.* 2014). Also, the structure of WSS lines have been used in developing theories for flow separation using dynamical system methods (Surana *et al.* 2006, 2008). Recently, WSS critical points associated with rare near wall backflow have been observed in turbulent channel flows (Lenaers *et al.* 2012; Brücker 2015). WSS patterns have been demonstrated to affect the heat transfer in impinging jets. As examples, the heat transfer coefficient has been shown to have similar distribution as WSS with a phase shift (Hadžiabdić & Hanjalić 2008), and Dairay *et al.* (2015) showed that the secondary vortex resulting from flow impingement creates negative WSS regions that correspond to heat transfer augmentation.

The correlations observed in the above studies between WSS and transport processes motivates more mechanistic exploration of near wall flow topology induced by the WSS vector field. In steady flows the critical points of the vector field and their associated invariant manifolds largely determine the flow topology. In unsteady flows Lagrangian coherent structures (LCS) have been used to obtain a template for transport (Shadden 2011; Haller 2015), including cardiovascular applications (Shadden & Taylor 2008; Shadden & Arzani 2015). These structures represent prominent flow features that organize the flow from a Lagrangian perspective. This study demonstrates the relevancy of similar structures obtained from the WSS vector field for organizing near wall transport in the context of patient specific AAA models. Namely, species accumulation in the boundary layer in connection with these structures will be demonstrated. The influence of diffusion and flow normal to the wall, is also investigated and discussed.

2. Methods

Velocity data was obtained from computational fluid dynamics (CFD) simulations of blood flow in two patient-specific AAA models, as described in Arzani *et al.* (2014*b*). The vascular models spanned from the descending aorta through the iliac arteries to ensure the region of interest (aneurysm) was sufficiently far from inflow and outflow boundaries. Major aortic branch arteries were also included due to their proximal influence on abdominal aortic flow. Inflow and outflow boundary conditions were tuned to match measured, patient-specific flow rates and blood pressures as described in Les *et al.* (2010). Rigid wall and Newtonian blood rheology were assumed. It has been shown that the Newtonian assumption produces reasonable WSS patterns in AAAs (Marrero *et al.* 2014) and that vessel deformation leads to relatively minor changes in overall flow topology (Duvernois *et al.* 2013). Figure 1 shows one of the two AAA models, to exemplify the anatomy of the model, morphology of volumetric flow waveform, and the nature of mesh. The results presented in this paper are mostly based on this model for demonstration purposes, although similar results were observed for other patient-specific geometries. The incompressible Navier-Stokes equations were solved using the stabilized finite element flow solver in SimVascular (simvascular.org). Linear tetrahedral elements, with second order time integration were used. The mesh edge size next to the wall was 200 μm, and the time step divided the cardiac cycle into 1000 time points. The peak Reynolds number was $Re = 1750$ and the Womersley number was $\alpha = 12.8$. The wall traction was obtained as $\boldsymbol{t} = \boldsymbol{\sigma} \cdot \boldsymbol{e}_n$, with the stress tensor $\boldsymbol{\sigma}$ and the unit normal vector $\boldsymbol{e}_n$ evaluated on the wall. The WSS vector was computed as

$$\boldsymbol{\tau} = \boldsymbol{t} - (\boldsymbol{t} \cdot \boldsymbol{e}_n)\boldsymbol{e}_n \ . \tag{2.1}$$

The convective near wall transport can be derived by Taylor expansion of the fluid velocity near the wall (Gambaruto *et al.* 2010) as

$$\boldsymbol{u}_\pi = \frac{\boldsymbol{\tau}\delta n}{\mu} + O(\delta n^2) \ , \tag{2.2}$$

where $\boldsymbol{u}_\pi$ is the velocity vector in the local wall tangent plane, μ is the dynamic viscosity, and the δn is the distance normal to the wall where the velocity is being evaluated.

The vector field defined by the first term on the right hand side of Eq. (2.2) was used to study transport. This vector field is defined on the surface mesh, however it represents the near wall fluid velocity (per Eq. 2.2), as fluid velocity is zero on the vessel surface itself due to the no-slip, no-penetration condition. To study transport on this simplicial complex (discrete surface manifold), the methods used in (Zhang *et al.* 2006; Chen *et al.* 2007) to obtain surface streamlines were extended to unsteady vector fields to obtain WSS surface pathlines. Pathlines were densely seeded over the aneurysm surface, and integrated for 100 cardiac cycles, or until they left the domain. After several cardiac cycles of flow simulation, the WSS vector field was recorded and assumed periodic since the inflow boundary condition was periodic. This enabled velocity data to be recycled for the purposes of trajectory integration over many cardiac cycles. The species concentration was assumed to be dilute and modeled by advection of non-interacting passive tracers.

In order to evaluate the regions of species accumulation in the boundary layer, we introduce a WSS exposure time measure, which is defined for each surface element
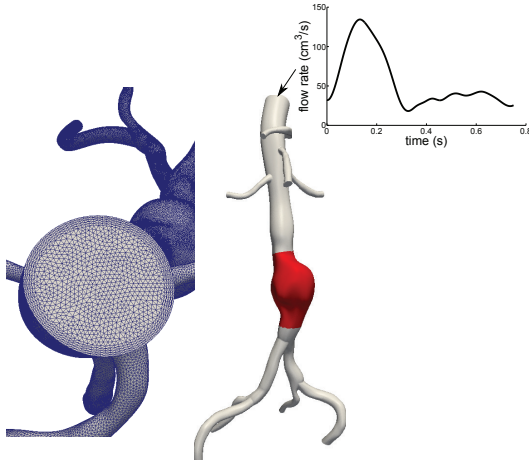
FIGURE 1. Example AAA model. The region of interest where trajectories are tracked is highlighted in red. The volumetric flow rate waveform at the inlet and the mesh are also shown. The first patient is shown in this figure.

(triangle) as the accumulated amount of time of all trajectories visiting that element

$$\text{WSS}_{ET}(e) = \sqrt{\tfrac{A_m}{A_e}} \sum_{p=1}^{N_t} \int_0^{\mathcal{T}} H_e(p, t) \, \mathrm{d}t \tag{2.3}$$

$$H_e = \begin{cases} 1 \text{ if } \boldsymbol{x}_p(t) \in e \\ 0 \text{ if } \boldsymbol{x}_p(t) \notin e \end{cases},$$

where A_e is the area of the element, A_m is the average area of all the elements, $\mathbf{x}_p(t)$ is the position of the near wall trajectory, H_e is the indicator function for element e, N_t is the total number of trajectories released, and $\mathcal{T}$ is the integration time. For each trajectory, we define the WSS residence time as the amount of time that it takes to leave the near wall flow domain, mapped back to the initial condition

$$\text{WSS}_{RT}(\mathbf{x}_0, t_0; \Gamma) = \min(t) \in (0, \mathcal{T}) \text{ s.t. } \mathbf{x}(\mathbf{x}_0, t_0 + t) \notin \Gamma , \tag{2.4}$$

where Γ is the near wall flow domain.

In order to characterize the near wall flow topology induced by the WSS vectors in complex geometries, one approach would be to compute the finite time Lyapunov exponent (FTLE) field on the lumen surface to identify LCS. In this study LCS were identified by simply advecting a large enough number of trajectories (≈ 42000) and identifying coherent structures formed. With sufficient forward time integration, the trajectories trace out prominent attracting LCS, and with backward time integration prominent repelling LCS are delineated. The motivation for this simple approach was to aid visualization; the temporal persistence of these near wall LCS made this possible. We refer to these as WSS LCS, which demonstrate organizing structures of near wall transport.

The above analysis ignores two effects that may be of importance. The reconstructed velocity in Eq. (2.2) ignores the normal near wall velocity. This velocity is second order, and is considered small close to the wall. However, over longer integrations in time this second order term might become important. The normal velocity can be written from

the same series expansion used above (Gambaruto *et al.* 2010) as

$$u_n = -\frac{1}{2\mu}\nabla \cdot \boldsymbol{\tau}\, \delta n^2 + O(\delta n^3)\,. \tag{2.5}$$

Thus, the divergence of WSS contributes to normal wall flux. Positive WSS divergence indicates flow towards the wall (e.g., impingement), and negative WSS divergence indicates flow away from the wall (e.g., separation).

The effect of diffusion on near wall transport is also ignored. A simple dimensional analysis shows that the diffusion in the wall normal direction is more significant than the streamwise diffusion. The normal diffusion in a Lagrangian framework can be modeled with a random walk approach (Ghosh *et al.* 1998)

$$\delta n(t + \Delta t) = \delta n(t) + \zeta \tag{2.6}$$
$$\zeta \sim \mathcal{N}(0,\, 2D\Delta t)\,,$$

where D is the mass diffusion coefficient, Δt is the integration time step, and ζ is a random variable determined from a Gaussian distribution, with zero mean and variance of $2D\Delta t$. In order to model the normal to the wall transport effects considered by Eq. (2.5) and Eq. (2.6), trajectories were confined to stay on the wall surface, however their normal-to-wall distance was tracked by these equations. Therefore, at each time step the trajectories experience a slightly different value of δn, which contributes to a different value for near wall velocity $\mathbf{u}_\pi$ (see Eq. 2.2) in addition to the inherent spatial and temporal change of the vector field. The normal to the wall transport was tracked until the trajectory left a near wall threshold ($\delta n_{\max}$), whereby the trajectory was assumed to be out of the near wall flow region where this model holds and the integration was terminated.

The near wall distance δn remains to be chosen. This distance needs to be chosen within the concentration boundary layer thickness δ_c. To approximate this, the order of magnitude of the momentum boundary layer thickness δ was evaluated from inspection of the thickness of the high vorticity region near the wall. The concentration boundary layer thickness was subsequently estimated using $\delta/\delta_c = Sc^{\frac{1}{3}}$ (Truskey *et al.* 2004). A mass diffusion coefficient of $D = 5 \times 10^{-6}\frac{cm^2}{s}$ was used, which is approximative of the diffusivity of chemicals and proteins in blood. The kinematic viscosity for blood was set to $\nu = 0.0377\ \frac{cm^2}{s}$, which gives a Sc number of $Sc = \frac{\nu}{D} \approx 7500$. Using the above estimates, the concentration boundary layer thickness was estimated as $\delta_c \approx 0.005$ cm. Since δn should be chosen within δ_c, a $\delta n = 0.0014\ cm$ was chosen. The sensitivity to this choice will be later discussed. The maximum near wall region thickness δn_{max} was chosen within the momentum boundary layer thickness δ in the region where the velocity profile was mostly linear ($\delta n_{max} \approx 0.05$ cm). A smaller δn_{max} was tested to ensure the results were not sensitive to this choice.

The full continuum 3D advection-diffusion problem was solved to validate the proposed Lagrangian surface transport approach. The advection-diffusion equation is written as

$$\frac{\partial c}{\partial t} + \boldsymbol{u} \cdot \nabla c = D\nabla^2 c\,, \tag{2.7}$$

where c is a non-dimensional concentration, $\boldsymbol{u}$ is the velocity and D is the mass diffusivity as above. A Neumann boundary condition of $\frac{\partial c}{\partial n} = 10\ cm^{-1}$ was prescribed at the no-slip wall representing a uniform flux of concentration. The inlet and outlet boundary conditions were set to $c = 0$. Zero Dirichlet outlet boundary condition was preferred to zero Neumann, due to the presence of reverse flow. The outlet boundary was extended to ensure minimal influence of the outlet boundary condition. A finite element method was used to solve the equation using streamline upwind/Petrov-Galerkin (SUPG) for-
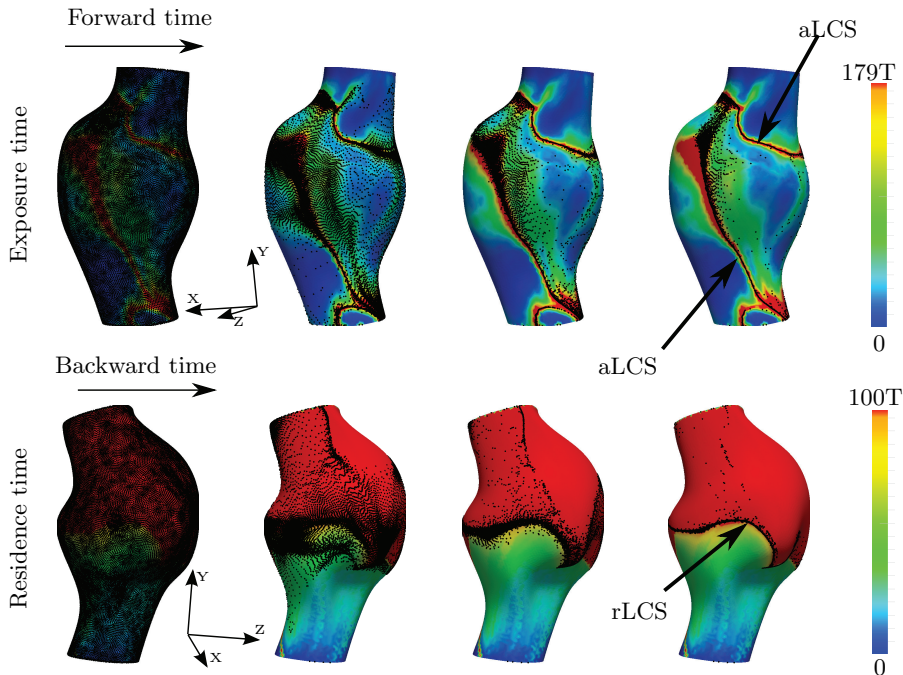
FIGURE 2. WSS exposure time and WSS residence time plots in first AAA model. Forward time trajectories are superimposed on the exposure time field, and backward time trajectories are superimposed on the residence time field. The forward and backward trajectories aggregate to attracting and repelling WSS LCS, respectively. $T = 0.75$ s is the cardiac cycle of the patient. The absolute time instances shown correspond to $t = 0$, $t = 27T$, $t = 61T$, and $t = 100T$ from left to right.

mulation (Brooks & Hughes 1982; Bazilevs *et al.* 2007), implemented in the FEniCS package (Logg *et al.* 2012). Second order tetrahedral elements were used with an edge size of 0.1 cm in the interior and a boundary layer mesh with next to wall edge size of 6.6 μm in order to resolve the concentration boundary layer. The simulation was run for 60 cardiac cycles until the surface concentration reached steady state.

3. Results

Figure 2 shows the WSS exposure time and WSS residence time fields in the first AAA model. Forward and backward time WSS trajectories are shown in the figure. In forward time (top row), WSS trajectories are seen to cluster towards distinct curves, which identify attracting WSS LCS. Trajectories remain in the vicinity of the attracting LCS for a long time, therefore the WSS exposure time is high in such regions. Moreover, the attracting LCS demonstrates little motion over time, which causes the region of high exposure time (red region in Fig. 2) to be confined to narrow bands. In backward time, WSS trajectories cluster to distinct curves, which identify a repelling WSS LCS. In this case the repelling LCS marks the boundary between the trajectories that eventually leave the domain, and those that remain in the near wall region for a long time (high residence time region).

Figure 3 further demonstrates the role of the WSS LCS in organizing near wall transport. The second patient is shown in this figure, due to interesting WSS LCS patterns. Three repelling WSS LCS, indicated by clustering of black tracers, divide the
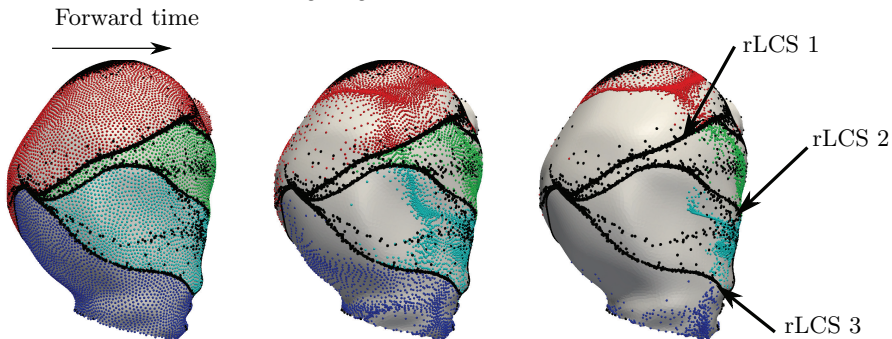
FIGURE 3. Three repelling WSS LCS are formed from backward time integration of WSS trajectories (black spheres). These LCS mark the boundary of four different near wall regions. Trajectories starting in each of these regions are colored differently, and are shown to have different fates. The second patient is shown in this figure. The time instances shown correspond to $t = 0$, $t = 34T$, and $t = 100T$ from left to right. $T = 0.95$ s is the cardiac cycle of this patient.

surface into four regions. Additional tracers are seeded and colored based on their initial position with respect to these regions. Upon advection of the colored sets of tracers it is seen that the trajectories starting in any of these four regions move collectively towards a different location in forward time. Namely, the repelling WSS LCS indicate boundaries between different basins of attraction for near wall species.

The effect of diffusion and normal velocity on near wall transport was modeled as described above and the results are shown in Fig. 4. The region of high WSS exposure time formed by the attracting WSS LCS remains robust with respect to these effects (top row). Diffusion causes some of the trajectories to leave the near wall domain in long integration times, therefore the exposure time is generally reduced, although the same features persist. Residence time results (bottom row) are more sensitive to diffusion and normal velocity effects. Diffusion causes trajectories to randomly leave the region of high residence time, and in general more noisy and lower residence time values are observed. However, the boundary between the region of high residence time and low residence time persists. Introduction of normal velocity leads to more dramatic change in the spatial distribution of residence time. This is for two reasons. First, the effect of normal flow is spatially dependent; in regions with large negative WSS divergence tracers will more quickly escape from the near wall region. Second, residence time, by its definition, is more sensitive to individual tracers leaving the near wall region. Alternatively, exposure time depends on the collective behavior of trajectories and is therefore less sensitive to this influence.

Next we consider the effect of different choices for δn on the results, as shown in Fig. 5. We note that the dynamic variation of δn is tacitly considered in the results of Fig. 4, however our goal here is to demonstrate more directly the underlying relationship of the flow behavior to near-wall distance. For small values of δn (top left) the WSS LCS is almost stationary, fluctuating in a very narrow region of high WSS exposure time. The reason for this quasi-steady behavior is that very close to the wall the WSS trajectories have a small velocity, thus have small displacements during one cardiac cycle, which is the time scale of flow unsteadiness. Subsequently, the near wall transport becomes quasi-steady with the time average (TA) WSS vector governing transport. Indeed, upon inspection of the limiting streamlines computed from the TAWSS vector field (bottom right), it can be observed that the attracting WSS LCS coincide with unstable manifolds of fixed points in the TAWSS vector field for small values of δn. For larger values of δn
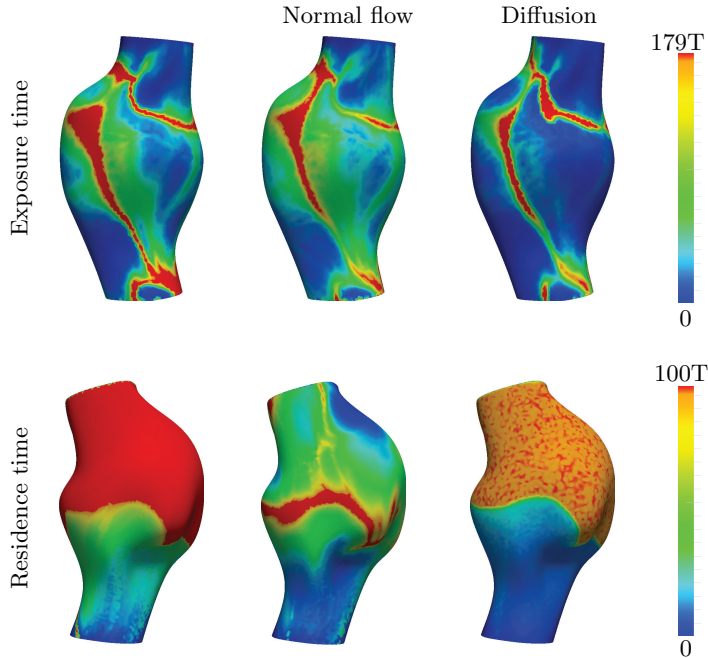
FIGURE 4. The effect of diffusion and normal flow on WSS exposure time and WSS residence time. $T = 0.75$ s is the cardiac cycle of the patient. Different views of the first patient is shown in this figure.

(top right and bottom left) it can be seen that the WSS LCS demonstrate increasing fluctuation with an increase in δn, as near wall convective transport becomes less stationary. However, for large Sc numbers, as long as δn is within δ_c the WSS LCS change modestly, and the WSS exposure time and residence time features are persistent.

To test the validity of using the first-order near-wall velocity approximation to integrate near-wall particle transport, Figure 6 compares the WSS exposure time derived from the surface transport model, and the surface concentration obtained from the full 3D advection-diffusion solution. The spatially averaged Sherwood number $Sh = \frac{\partial c}{\partial n} d \ / (C_s - C_i)$, where d is the maximum aneurysm diameter, C_s is the (spatially averaged) surface concentration, and $C_i = 0$ is the inlet concentration, was found to be 387. Relative agreement can be observed between the main features (identified hot spots) using the two approaches, validating the surface-based Lagrangian approach. To establish convergence of the numerical results, Figure 7 shows a comparison of the baseline TAWSS streamlines and WSS LCS to those derived from a Navier-Stokes solution using a finer mesh with next to wall edge size of 100 μm. Relatively minor change in the structures are observed, indicating adequate near-wall resolution of the flow field solution.

4. Discussion

In this study the role of Lagrangian wall shear stress structures on organizing the near wall transport of high Sc flows was investigated in the context of blood flow in abdominal aortic aneurysm. It was shown that the attracting and repelling WSS LCS act as templates of near wall transport. The applicability of this approach relies on the existence of a thin concentration/thermal boundary layer. Using δ to scale the normal to wall distance, the relative error in neglecting the higher order terms in Eq. (2.2) is
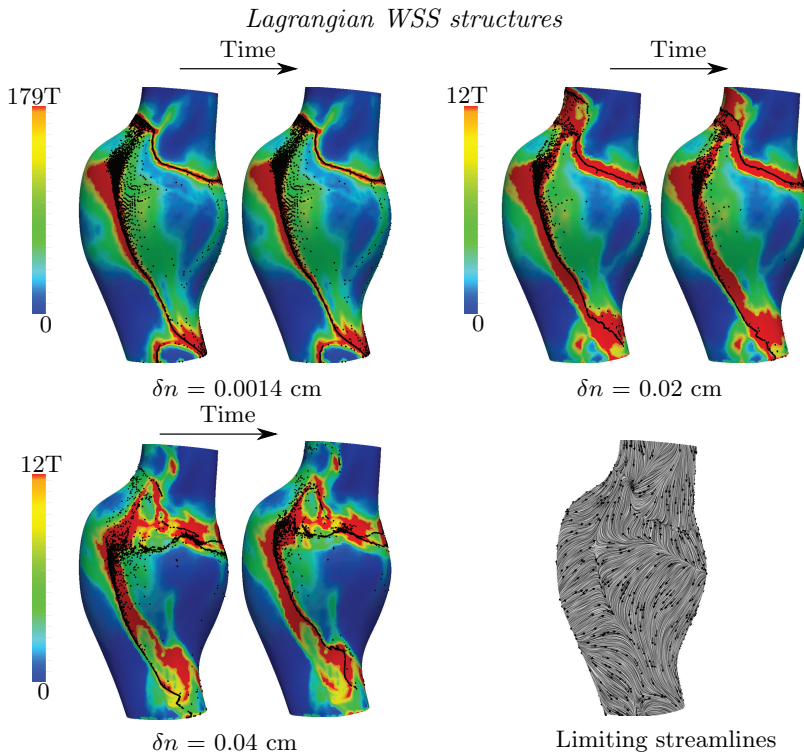
FIGURE 5. WSS exposure time contours with the attracting WSS LCS (indicated by particle clustering) for different values of δn in the first patient. Two different time instances are shown to visualize the extremes in temporal displacement of the LCS. The limiting streamlines of the TAWSS vector field are also shown, with normalized arrows showing the direction of WSS vectors. For smaller δn, the attracting LCS demonstrate less movement and are well-approximated by the unstable manifolds of the TAWSS vector field. For larger δn, near wall transport, and hence WSS LCS, become more unsteady. $T = 0.75$ s is the cardiac cycle for the patient. The two time instances shown differ by 2T.
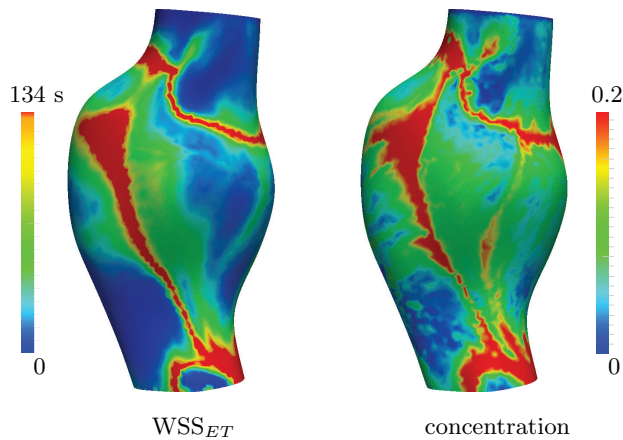

FIGURE 6. Comparison of WSS exposure time (WSS_{ET}) with the non-dimensional surface concentration obtained from the corresponding 3D continuum advection-diffusion equation.
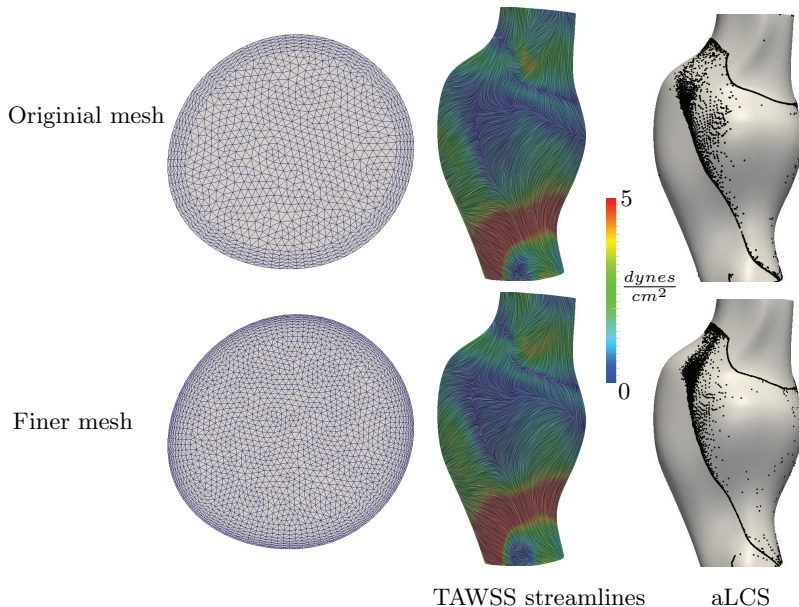
Figure 7. Comparison of the TAWSS streamlines and attracting LCS (aLCS) obtained from the original mesh (next to wall edge size 200 μm) to a finer mesh (next to wall edge size 100 μm) in the first patient. The TAWSS streamlines are colored based on the TAWSS vector magnitude.

$O(\frac{\delta n}{\delta})$. δn is chosen as the same order as δ_c, therefore the relative error in the linear approximation is $O(\frac{\delta_c}{\delta})$. A relative error of 10% gives $Sc \approx 1000$. Therefore, the current approach may give reasonable results for Sc or Pr number $O(10^3)$ or higher (in the examples shown $Sc \approx 7500$). We note however that the second order term scales with WSS divergence, thus the near wall transport model can break down in locations of high WSS divergence (cf. Fig. 4).

It has been shown that for $Sc \gtrsim O(10^3)$ mass transfer resulting from unsteady blood flow was similar to that obtained from the time-averaged components (Ma *et al.* 1994). Our result are consistent and provide further explanation. Two different time scales govern the near wall transport. The time scale for variations in the base flow (one cardiac cycle) is much smaller than the time scale for effective transport of near wall species (several cardiac cycles), implying that near wall transport is quasi-steady. It is important to keep in mind that in complex flows a time-dependent flow solve is still needed, as the time-averaged WSS field obtained from the time-dependent flow can be different from the WSS field obtained from a steady simulation with a time-averaged inflow. For the flow conditions considered in this study, we verified that using the TAWSS vector as a steady vector produced nearly identical WSS_{ET} results to the corresponding unsteady WSS vector field. Our results also demonstrated that the quasi-steady behavior of near wall transport led to the conforming of the WSS LCS with the stable/unstable manifolds of the TAWSS vector field. Moreover, Shariff *et al.* (1991) have shown that stable/unstable manifolds in the velocity field emerge from critical points of the time-averaged WSS field in periodic two-dimensional flows. Therefore, the relation between WSS critical points and their invariant manifolds with the core flow features can provide insight into the basis of near wall transport.

For high Sc, as long as δn was chosen within the concentration boundary layer, the exact choice did not significantly affect the qualitative behavior of the WSS LCS, WSS

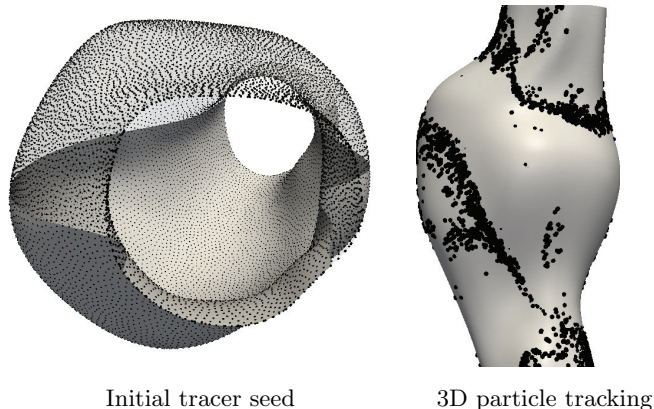Initial tracer seed   3D particle tracking

FIGURE 8. Tracers are seeded near the wall ($\delta n = 7\mu m$) and integrated in forward time using the first patient model. The left panel shows tracer seed locations. The right panel shows the emerging near wall structures after sufficient forward 3D integration. (Particles on right are enlarged to become visual through the surface.)

exposure time and residence time fields. We note that a decrease in Sc number yields a larger concentration boundary layer thickness, and subsequently more unsteadiness in near wall transport manifested in the temporal variations of WSS LCS. In the case of smaller Sc number flows, a higher order representation of the near wall flow by means of a series expansion (Perry & Chong 1986) may be employed to accurately model the near wall transport with a larger δn. In this case, depending on the Sc number it is likely that the trajectories closer to the wall will be controlled by the time-averaged WSS vector field manifolds, and trajectories further away from the wall will be subject to unsteadiness around these manifolds (cf. Fig.5).

While one may use the full 3D velocity field to track near wall tracers, this can be difficult to implement. For validation, we seeded tracers $\delta n = 7\mu m$ from the wall and integrated them forward in time using the full 3D flow field until coherent structures were formed near the wall as shown in Fig. 8. It can be observed that tracers accumulate near the same attracting WSS LCS as shown in Fig. 2. However, in using the 3D velocity field for integrating near wall tracers, small errors in numerical integration are more easily amplified. Namely, such errors result in (1) increases in δn causing higher normal velocities and tracers leaving the near-wall region prematurely, or (2) decreases in δn causes tracers to stick to, or penetrate, the wall. Over long integration times needed to understand near wall transport, the accuracy of near wall integration can become significantly impaired due to these effects. Alternatively, the surface integration method provides a more efficient approach, while maintaining accuracy as for example demonstrated by the agreement between WSS_{ET} and the surface concentration obtained from solving the 3D continuum advection-diffusion equation (cf. Fig.6).

For most vascular applications, the emergent WSS LCS patterns will be largely dependent on the vascular geometry and Reynolds and Womersley numbers as these factor most influence flow topology. Indeed, Gopalakrishnan *et al.* (2014) have shown that small changes in the AAA geometry can significantly affect the WSS distribution, and changes in the curvature of the vessel wall have also been shown to affect WSS (Siggers & Waters 2008). In the current study we demonstrated results in two patient geometries, however, we also performed similar simulations in a total of six patient geometries and observed similar WSS LCS structures influencing the observed near wall concentration fields. Thus, the indication that Lagrangian wall shear stress structures can provide a

template for near wall transport appears to hold generally over widely varying geometrical models.

The inlet flow waveforms used in this study were patient specific resting waveforms obtained from phase contrast magnetic resonance measurements. We have performed preliminary study on the effect of simulated exercise flow conditions (increased Reynolds and Womersley numbers, as modeled in Arzani *et al.* (2014*a*)) on WSS LCS, and observed that the quasi-steady behavior of near wall transport can break down due to the higher WSS magnitudes. In addition, pulsatile blood flow may have some cycle to cycle variations due to transient effects from the fluid mechanics or physiology. In this study we assumed a periodic WSS vector field to generate WSS trajectories. Depending on the Reynolds and Womersley numbers, the intercycle variations in the flow field can break down the quasi-steady behavior of the WSS LCS, leading to greater unsteadiness in the near wall transport. Under such conditions the WSS LCS may demonstrate time dependent behavior and deviate from the stable/unstable manifolds of the TAWSS field. Additional considerations that remain to be studied are that higher WSS divergence magnitudes typically observed under exercise conditions, as well as physiologic deformation of the vessel wall due to wall compliance, may increase transport normal to the vessel wall in the boundary layer. To visualize the WSS LCS in this study we relied on a simple advection of tracers. Alternatively, one could compute the finite-time Lyapunov exponents (FTLE) on a non-Euclidean manifold to visualize the LCS (Lekien & Ross 2010). The simple approach employed here is nonetheless able to identify the more prominent LCS, which affect the concentration pattern on the vessel surface.

The current study provides a framework for understanding the mechanisms underlying mass/heat flux at a no-slip wall in disturbed high Sc/Pr flows. In particular, attracting WSS LCS determine patterns of high species concentration, and repelling WSS LCS mark the boundaries of different basins of attraction. Therefore, the WSS LCS provide a template for the distribution and evolution of wall generated species. Recently, Nguyen *et al.* (2015) have demonstrated the separation between near wall species with different Sc numbers. This separation could also happen due to the partitioning effect of the repelling WSS LCS as demonstrated in Fig 3. From a design perspective, it would be interesting to manipulate these structures to obtain a WSS pattern with a desired outcome of wall concentration/temperature distribution, in similar fashion to Hubble *et al.* (2013), who investigated the effect of vortical structures near the boundary layer on heat transfer augmentation. Finally, the bearing of these structures on near wall transport of turbulent flows remains to be investigated.

Acknowledgements

REFERENCES

Arzani, A., Les, A. S., Dalman, R. L. & Shadden, S. C. 2014*a* Effect of exercise on patient specific abdominal aortic aneurysm flow topology and mixing. *International journal for numerical methods in biomedical engineering* **30** (2), 280–295.

Arzani, A. & Shadden, S. C. 2012 Characterization of the transport topology in patient-specific abdominal aortic aneurysm models. *Physics of Fluids* **24** (8), 1901.

ARZANI, A., SUH, G. Y., DALMAN, R. L. & SHADDEN, S. C. 2014*b* A longitudinal comparison of hemodynamics and intraluminal thrombus deposition in abdominal aortic aneurysms. *American Journal of Physiology-Heart and Circulatory Physiology* **307** (12), H1786–H1795.

BAZILEVS, Y., CALO, V. M., TEZDUYAR, T. E. & HUGHES, T. J. R. 2007 Yzβ discontinuity capturing for advection-dominated processes with application to arterial drug delivery. *Int J Numer Methods Fluids* **54**, 593–608.

BROOKS, A. N. & HUGHES, T. J. R. 1982 Streamline upwind/Petrov-Galerkin formulations for convection dominated flows with particular emphasis on the incompressible Navier-Stokes equations. *Computer methods in applied mechanics and engineering* **32** (1), 199–259.

BRÜCKER, C. 2015 Evidence of rare backflow and skin-friction critical points in near-wall turbulence using micropillar imaging. *Physics of Fluids (1994-present)* **27** (3), 031705.

CARDESA, J. I., MONTY, J. P., SORIA, J. & CHONG, M. S. 2014 Skin-friction critical points in wall-bounded flows. In *Journal of Physics: Conference Series*, , vol. 506, p. 012009.

CHEN, G., MISCHAIKOW, K., LARAMEE, R. S., PILARCZYK, P. & ZHANG, E. 2007 Vector field editing and periodic orbit extraction using morse decomposition. *Visualization and Computer Graphics, IEEE Transactions on* **13** (4), 769–785.

DAIRAY, T, FORTUNÉ, V, LAMBALLAIS, E & BRIZZI, L. E. 2015 Direct numerical simulation of a turbulent jet impinging on a heated wall. *Journal of Fluid Mechanics* **764**, 362–394.

DEPLANO, V., KNAPP, Y., BERTRAND, E. & GAILLARD, E. 2007 Flow behaviour in an asymmetric compliant experimental model for abdominal aortic aneurysm. *Journal of Biomechanics* **40**, 2406–2413.

DUVERNOIS, V., MARSDEN, A. L. & SHADDEN, S. C. 2013 Lagrangian analysis of hemodynamics data from FSI simulation. *International Journal for Numerical Methods in Biomedical Engineering* **29** (4), 445–461.

EL HASSAN, M., ASSOUM, H. H., MARTINUZZI, R., SOBOLIK, V., ABED-MERAIM, K. & SAKOUT, A. 2013 Experimental investigation of the wall shear stress in a circular impinging jet. *Physics of Fluids (1994-present)* **25** (7), 077101.

ETHIER, C. R. 2002 Computational modeling of mass transfer and links to atherosclerosis. *Annals of biomedical engineering* **30** (4), 461–471.

FINOL, E. A. & AMON, C. H. 2001 Blood flow in abdominal aortic aneurysms: pulsatile flow hemodynamics. *Journal of Biomechanical Engineering* **123** (5), 474–484.

GAMBARUTO, A. M., DOORLY, D. J. & YAMAGUCHI, T. 2010 Wall shear stress and near-wall convective transport: Comparisons with vascular remodelling in a peripheral graft anastomosis. *Journal of Computational Physics* **229** (14), 5339–5356.

GHOSH, S., LEONARD, A. & WIGGINS, S. 1998 Diffusion of a passive scalar from a no-slip boundary into a two-dimensional chaotic advection field. *Journal of Fluid Mechanics* **372**, 119–163.

GOPALAKRISHNAN, S. S., PIER, B. & BIESHEUVEL, A. 2014 Dynamics of pulsatile flow through model abdominal aortic aneurysms. *Journal of Fluid Mechanics* **758**, 150–179.

HADŽIABDIĆ, M & HANJALIĆ, K 2008 Vortical structures and heat transfer in a round impinging jet. *Journal of Fluid Mechanics* **596**, 221–260.

HALLER, G. 2015 Lagrangian coherent structures. *Annual Review of Fluid Mechanics* **47**, 137–162.

HUBBLE, D. O., VLACHOS, P. P. & DILLER, T. E. 2013 The role of large–scale vortical structures in transient convective heat transfer augmentation. *Journal of Fluid Mechanics* **718**, 89–115.

LEKIEN, F. & ROSS, S. D 2010 The computation of finite-time Lyapunov exponents on unstructured meshes and for non-Euclidean manifolds. *Chaos: An Interdisciplinary Journal of Nonlinear Science* **20** (1), 017505.

LENAERS, P., LI, Q., BRETHOUWER, G., SCHLATTER, P. & ÖRLÜ, R. 2012 Rare backflow and extreme wall-normal velocity fluctuations in near-wall turbulence. *Physics of Fluids (1994-present)* **24** (3), 035110.

LES, A. S., SHADDEN, S. C., FIGUEROA, C. A., PARK, J. M., TEDESCO, M. M., HERFKENS, R. J., DALMAN, R. L. & TAYLOR, C. A. 2010 Quantification of hemodynamics in abdominal aortic aneurysms during rest and exercise using magnetic resonance imaging and computational fluid dynamics. *Annals of Biomedical Engineering* **38** (4), 1288–1313.

LOGG, A., MARDAL, K. A. & WELLS, G. 2012 *Automated solution of differential equations by the finite element method*, , vol. 84. Springer, Berlin, Heidelberg.

MA, P., LI, X. & KU, D. N. 1994 Heat and mass transfer in a separated flow region for high prandtl and schmidt numbers under pulsatile conditions. *International journal of heat and mass transfer* **37** (17), 2723–2736.

MARRERO, V. L., TICHY, J. A., SAHNI, O. & JANSEN, K. E. 2014 Numerical study of purely viscous non-Newtonian flow in an abdominal aortic aneurysm. *Journal of Biomechanical Engineering* **136** (10), 101001.

NGUYEN, Q., SRINIVASAN, C. & PAPAVASSILIOU, D. V. 2015 Flow-induced separation in wall turbulence. *Physical Review E* **91** (3), 033019.

PERRY, A. E. & CHONG, M. S. 1986 A series-expansion study of the navier–stokes equations with applications to three-dimensional separation patterns. *Journal of fluid mechanics* **173**, 207–223.

PERRY, A. E. & CHONG, M. S. 1987 A description of eddying motions and flow patterns using critical-point concepts. *Annual Review of Fluid Mechanics* **19** (1), 125–155.

SALSAC, A. V., SPARKS, S. R., CHOMAZ, J. M. & LASHERAS, J. C. 2006 Evolution of the wall shear stresses during the progressive enlargement of symmetric abdominal aortic aneurysms. *Journal of Fluid Mechanics* **560**, 19–52.

SHADDEN, S. C. 2011 Lagrangian coherent structures. In *Transport and Mixing in Laminar Flows: From Microfluidics to Oceanic Currents*. Wiley-VCH Verlag GmbH & Co. KGaA.

SHADDEN, S. C. & ARZANI, A. 2015 Lagrangian postprocessing of computational hemodynamics. *Annals of Biomedical Engineering* **43** (1), 41–58.

SHADDEN, S. C. & TAYLOR, C. A. 2008 Characterization of coherent structures in the cardiovascular system. *Annals of Biomedical Engineering* **36**, 1152–1162.

SHARIFF, K., PULLIAM, T. H. & OTTINO, J. M. 1991 A dynamical systems analysis of kinematics in the time-periodic wake of a circular cylinder. *Lect. Appl. Math* **28**, 613–646.

SIGGERS, J. H. & WATERS, S. L. 2008 Unsteady flows in pipes with finite curvature. *Journal of Fluid Mechanics* **600**, 133–165.

SUH, G. Y., LES, A. S., TENFORDE, A. S., SHADDEN, S. C., SPILKER, R. L., YEUNG, J. J., CHENG, C. P., HERFKENS, R. J., DALMAN, R. L. & TAYLOR, C. A. 2011*a* Quantification of particle residence time in abdominal aortic aneurysms using magnetic resonance imaging and computational fluid dynamics. *Annals of Biomedical Engineering* **39**, 864–883.

SUH, G. Y., TENFORDE, A. S., SHADDEN, S. C., SPILKER, R. L., CHENG, C. P., HERFKENS, R. J., DALMAN, R. L. & TAYLOR, C. A. 2011*b* Hemodynamic changes in abdominal aortic aneurysms with increasing exercise intensity using MR exercise imaging and image-based computational fluid dynamics. *Annals of Biomedical Engineering* **39**, 2186–2202.

SURANA, A., GRUNBERG, O. & HALLER, G. 2006 Exact theory of three-dimensional flow separation. part 1. steady separation. *Journal of fluid mechanics* **564**, 57–103.

SURANA, A., JACOBS, G. B., GRUNBERG, O. & HALLER, G. 2008 An exact theory of three-dimensional fixed separation in unsteady flows. *Physics of Fluids (1994-present)* **20** (10), 107101.

TRUSKEY, G. A., YUAN, F. & KATZ, D. F. 2004 *Transport phenomena in biological systems*. Pearson/Prentice Hall Upper Saddle River NJ:.

ZHANG, E., MISCHAIKOW, K. & TURK, G. 2006 Vector field design on surfaces. *ACM Transactions on Graphics (TOG)* **25** (4), 1294–1326.